Electrical Submersible Pumps: A System Modeling Approach for Power Quality Analysis With Variable Frequency Drives

P. M. Lingom, *Student Member, IEEE*, Joseph Song-Manguelle, *Senior Member, IEEE*, Mamadou Lamine Doumbia, *Member, IEEE*, Rodolfo César Costa Flesch, *Member, IEEE*, and Tao Jin, *Senior Member, IEEE*

***Abstract*—This article proposes a high-level engineering guide to develop an integrated system model for power quality analysis in electrical submersible pump (ESP) applications with variable frequency drives (VFDs). Such analyses are troublesome in the industry due to the complexity of these systems. In this article, simple steps to perform system integration analyses of such arrangements, including torsional analysis, are developed. A simplified VFD-ESP model suitable for coupled electrical and mechanical analysis in steady state is proposed in all their configurations of practical interest. Such a model can be easily implemented in common simulation software, significantly reducing engineering efforts for implementation and analysis. The focus of the proposed model is the prediction of ESP failures that might result from a poor power quality caused by VFDs. Analytical expressions of different types of harmonics in these systems, as well as their accurate locations in the frequency domain, including their interharmonics and common-mode harmonics, are derived for this purpose. The effectiveness of the proposed model is verified through offline and real-time hybrid simulation results. Finally, a comparison between simulation results obtained using the proposed model and measurements collected on a down-scale laboratory prototype is carried out to demonstrate the accuracy of the suggested modeling approach.**

***Index Terms*—Electrical submersible pumps (ESP), harmonics, power quality (PQ), system modeling, variable frequency drives (VFDs).**

Manuscript received April 1, 2021; revised September 8, 2021 and October 26, 2021; accepted November 27, 2021. Date of publication December 9, 2021; date of current version February 18, 2022. This work was supported by the Chinese National Natural Science Foundation under Grants 51977039 and 51950410593. Recommended for publication by Associate Editor G. Konstantinou. *(Corresponding author: Tao Jin.)*

P. M. Lingom and Tao Jin are with the Department of Electrical Engineering, Fuzhou University, Fuzhou 350116, China (e-mail: filslingom@yahoo.com; jintly@fzu.edu.cn).

Joseph Song-Manguelle is with the National Transportation Research Center, Oak Ridge National Laboratory, Knoxville, TN 37932 USA (e-mail: songmanguelj@ornl.gov).

Mamadou Lamine Doumbia is with the Department of Electrical and Computer Engineering, University of Quebec, Trois-Rivieres, QC G8Z 4M3, Canada (e-mail: mamadou.doumbia@uqtr.ca).

Rodolfo César Costa Flesch is with the Department of Automation and Systems, Federal University of Santa Catarina, Santa Catarina 88040-900, Brazil (e-mail: rodolfo.flesch@ufsc.br).

Color versions of one or more figures in this article are available at https://doi.org/10.1109/TPEL.2021.3133758.

Digital Object Identifier 10.1109/TPEL.2021.3133758

I. Introduction

THIS article is about system integration involving rotating machinery, such as fans, pumps, compressors, turbines, and electric motors, supplied by variable frequency drives (VFDs). It specifically covers system integration issues involving both the VFD and the transmission cable, such as in electrical submersible pumps (ESP) applications or single-load long tieback subsea pump applications [1], [2]. In such systems, the VFD is topside, and the motor is submerged at a distance to a motor that can exceed 30 km [3].

In general, two main VFD configurations are typically used in ESP applications: a low-voltage (LV) VFD with a step-up transformer and a medium-voltage (MV) VFD without a step-up transformer [4]. LV-VFD is a typical configuration for onshore ESP applications, while MV-VFD is the preferred one for offshore production facilities [5]. Both systems are also used in other submarine applications for distances greater than 30 km and for motor loads up to 3 MW [6].

An ESP setup consists of a set of components: an optional input transformer to connect the VFD to the network utility, the VFD (power and control parts), an optional output filter, the step-up transformer to be connected at the output of the VFD, an underground transmission cable, a motor lead extension cable, the connector, and a penetrator to insure a dry connection between the cable and the immersed motor [7]. Each individual component is usually designed and tested by each manufacturer according to the agreed design specifications, which fulfill the applicable industry and international standards [8]. However, the installation and integration of all these components are quite challenging, which may lead to premature system failures [9].

Most of the reported ESP failures have been linked to the VFD-induced harmonics and other aspects of poor power quality (PQ) caused by VFD-generated waveforms [10], [11]. Engineering time for such analysis might significantly increase the price of the system to be installed or modified [12]. One of the reasons for such cost increase is the segregation of engineering tasks in the industry. The design, integration, and tests of rotating machinery shaft systems are usually performed by mechanical engineers, while the design and test of VFD systems are performed by electrical engineers [13]. Most of the published documentation also exhibits the industry segregation between

electrical and mechanical engineering fields. On the one side, mechanical engineering publications around machine vibrations are mainly focused on rotor dynamics (mode shape, critical speeds, shear stress, etc.) [14]–[16], which are quite complex to be linked by electrical engineers to their activities, such as VFD harmonics evaluation. And on the other side, electrical engineering publications on VFDs are also written for electrical engineering issues (VFD topologies and their control strategies, for example) [17], [18]. These topics are substantially complex to be linked by mechanical engineers to their routine tasks, such as torsional vibration analysis.

To date, there are no IEEE standards that VFD supplying load at a tieback distance of 1 km and greater shall fulfill to guarantee no PQ related failures [19]. Also, a search of the literature did not reveal an integrated system model for investigating the PQ issues in VFD-ESP systems. One way to possibly understand and study such issues is to analyze the system using a computer-aided simulation tool [20]. The conventional approach for such a study is based on modeling the complete ESP power system in a computer software environment, where VFD power topology, including power switches, step-up transformer, transmission cable, electrical machine, and pump model are connected [21]–[23]. The development and implementation of such a simulation model can be troublesome for field engineers. They also pose many challenges, especially if different VFD-ESP systems with a wide range of operating conditions have to be investigated, such as the long simulation time, the need to wait for each system to reach its steady state for an accurate analysis, the need for accurate knowledge of each specific VFD topology internal operation, and the need to implement each manufacturer control strategy, which is often based on proprietary knowledge. Hence, it is beneficial for practicing and field engineers who are involved in the design, selection, integration, and retrofit of ESP components and systems to possess an easy-to-use tool to perform high-level system integration analysis of their installations.

To this end, this article proposes a simplified and generalized VFD-ESP model suitable for coupled electrical and mechanical resonance analysis in steady state. The proposed model does not require a deep knowledge of the VFD operation and can be easily implemented in common simulation software; thus, providing a lot of flexibility to alter a VFD-ESP system operation to suit different scenarios at reduced time. Such an approach is important in the design stage, particularly regarding the prediction of the possible operating points where electrical and mechanical resonance modes are located so that the risk of operating at those points can be avoided.

For the purpose of efficient development of the proposed model, an ESP system with two-level, three-level neutral point clamped (NPC) and *N*-level cascaded H-bridge (CHB) converters are investigated in this article. These VFD topologies are the most used in ESP applications [25]. To build the proposed model, a simple and unified modeling approach to explain how VFDs can excite either electrical resonance modes of a transmission cable or mechanical resonance modes of a rotating shaft in multi-inertia systems is first proposed. Second, a simple and straightforward approach to mimic a VFD output waveform without understanding its internal behavior is proposed. Finally, a simple analytical approach to reconstruct the torque dynamic behavior in ESP motor airgap is suggested. Finally, analytical expressions of different types of VFD-induced harmonics in these systems are derived. Such developments will define theoretical harmonic families at the output of the VFD so that differential and common mode harmonic components can be identified.

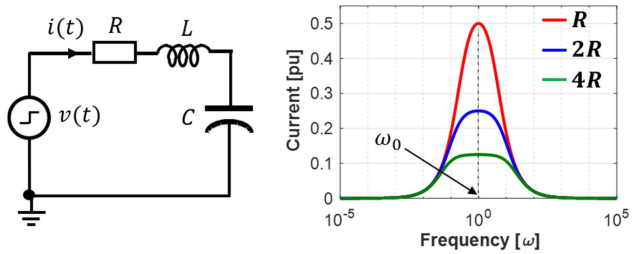

(a) (b)

Fig. 1. Resonance phenomenon in an electrical circuit. (a) Basic *RLC* circuit. (b) Resonance curve.

The rest of this article is organized as follows. Section II separately explains the resonance phenomena both in electrical circuits and in rotating mechanical shafts while highlighting their similarities. Section III presents the detailed description of the proposed simplified VFD-ESP model. Analytical expressions of different types of harmonics in these systems are derived and discussed in Section IV. Numerical and experimental results are provided and discussed in Section V. Finally, Section VI concludes this article.

II. Resonance Phenomena in Electrical and Mechanical Systems

A. Resonance Phenomenon in Electrical System

1) Basic Considerations: RLC Circuit: Fig. 1(a) shows a basic series *RLC* circuit with resistance R, inductance L, and capacitance C. Applying Kirchhoff's voltage law to Fig. 1(a) gives the following relationships:

$$L\frac{di}{dt} + Ri\left(t\right) + \frac{1}{C}\int i\left(t\right)dt = v\left(t\right) \tag{1a}$$

$$\frac{di^2\left(t\right)}{dt^2} + 2n\frac{di}{dt} + k^2 i\left(t\right) = 0 \tag{1b}$$

$$n = \frac{R}{2L}; k^2 = \frac{1}{LC} \tag{1c}$$

where $k = \omega_0$ is the system's natural frequency given by

$$L\omega_0 - \frac{1}{C\omega_0} = 0 \Rightarrow \omega_0 = \frac{1}{\sqrt{LC}}. \tag{2}$$

At that frequency, there is a continuous energy exchange between L and C such that the energy stored in the inductor is transferred to the capacitor, and then transferred back to the inductor, and so on. This phenomenon is called resonance. In such conditions, the current is only limited by the resistance, as shown in Fig. 1(b), for different values of R. This energy exchange creates a power oscillation into the circuit. The current

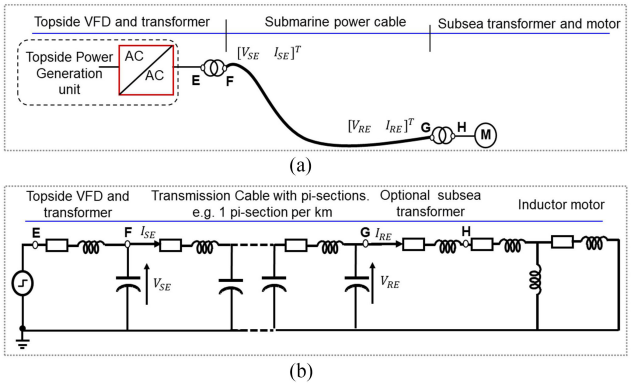

Fig. 2. Long tieback system. (a) Single-line diagram. (b) Electrical model.

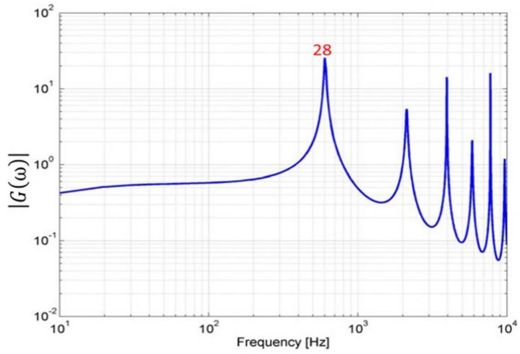

Fig. 3. Sample frequency simulation result of a transmission cable transfer function.

magnitude reaches its maximum value at that resonance frequency. This value can be significantly high compared with the current value at frequencies located far away from the resonance frequency.

2) Circuit With Multiple LC Branches: Transmission Cable: Fig. 2(a) shows a generic example of an ESP system configuration circuit, which is currently used in the oil and gas industry in general. Fig. 2(b) shows a simplified single-phase electric model of the system for electrical resonance investigation. The VFD is represented as a controlled voltage source, as explained in Section III-B. The transformer is represented by its *RL* impedance, and the motor is also represented by its steady-state impedance [26]. The transmission cable is represented as multiple pi-section networks (e.g., one pi-section per kilometer).

Because there are multiple *LC* branches, the system shown has multiple resonance frequencies. These frequencies can be found with a frequency sweep on one end of the system. The system impedance seen at the output of the VFD has multiple minima and maxima. All the frequencies where this impedance reaches a minimum value are considered as resonance frequencies. When the impedance reaches a maximum, those frequencies are considered antiresonance frequencies. At these frequencies, the voltage or the current may reach very high values. Fig. 3 shows a sample frequency sweep simulation result in the form of the system gain in steady-state such that

$$|G(\omega)| = \frac{V_{RE}}{V_{SE}} \tag{3}$$

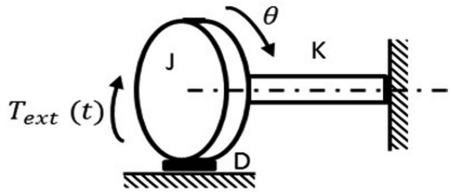

Fig. 4. Single inertia rotating mechanical system.

where V_{SE} and V_{RE} are the cable's sending and receiving ends and the investigated system consists of an MV VFD supplying an ESP motor rated 6.6 kV through a long cable. It can be observed that if the VFD is able to generate a voltage harmonic located approximately at 510 Hz with a magnitude of 1 kV, then the motor will be supplied with an overvoltage of 28 kV, which is far higher than its nominal value. In a real system, the cable skin effect will increase the transmission cable resistance as the frequency increases, acting therefore as a system with high damping. However, the VFD may still excite the system's electric impedance, potentially leading to a high overvoltage.

B. Resonance Phenomenon in Mechanical System

1) Basic Considerations: Rotating System With One Inertia: Fig. 4 shows a rotating mechanical system with one inertia $\boldsymbol{J}$, one damping coefficient $\boldsymbol{D}$, and one stiffness constant $\boldsymbol{K}$.

The shaft's angular position is denoted by θ. Applying Newton's second law to the system gives

$$\frac{\mathrm{d}\theta^2(t)}{\mathrm{d}t^2} + 2n\frac{\mathrm{d}\theta}{\mathrm{d}t} + k^2\theta = \frac{t_{\mathrm{ext}}}{J} \tag{4a}$$

$$n = \frac{D}{2K}; k^2 = \frac{1}{K/J}. \tag{4b}$$

This equation is identical to (1) given for an *RLC* circuit. To better analyze the system equation, first, the case where the system has no damping and the external applied torque T_{ext} is a harmonic defined such that

$$T_{\mathrm{ext}}(t) = T_a \sin(\omega_{\mathrm{nat}} t). \tag{5}$$

In that case, the parameters are to be set as follows:

$$n = 0 \tag{6}$$

$$k = \omega_{\mathrm{nat}}.$$

Solving the differential equation yields

$$\theta(t) = \frac{T_a}{2\omega_{\mathrm{nat}}}\left(\frac{1}{\omega_{\mathrm{nat}}}\sin(\omega_{\mathrm{nat}} t) - t\cos(\omega_{\mathrm{nat}} t)\right). \tag{7}$$

According to (7), it is noticed that if an external torque component is applied to the shaft system with a frequency equal to the natural frequency of the shaft; the resulting shaft's position has two components: 1) one having the same pulsation as the shaft's natural frequency ω_{nat} and a constant magnitude: $T_a/2\omega_{\mathrm{nat}}^2$; 2) another one also having the same pulsation as the natural frequency of the system but with proportionally time-varying magnitude: $t(T_a/2\omega_{\mathrm{nat}})$. Therefore, even for a small external torque magnitude, the amplitude of this component increases with time. Fig. 5 illustrates the mechanism of excitation of a shaft

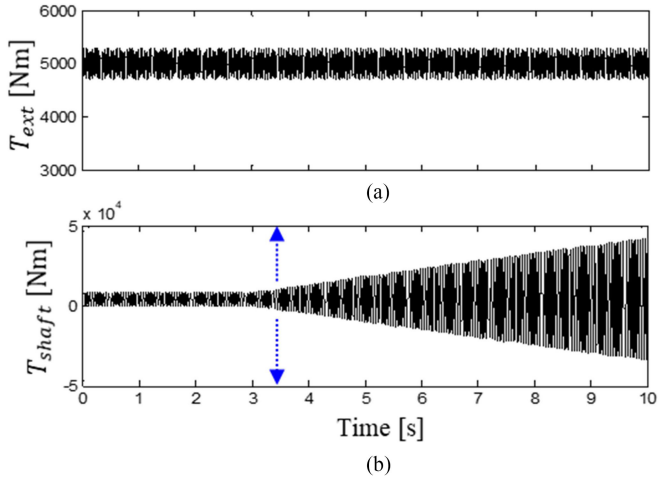

Fig. 5. Example of a shaft excited at one of its natural frequencies. (a) Motor air gap torque. (b) Resultant torque on the shaft.

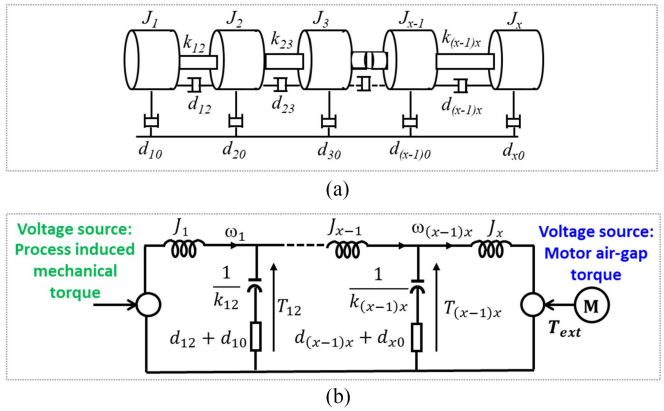

Fig. 6. Generic shaft system and its electrical equivalent circuit. (a) Generic shaft system. (b) Equivalent electrical circuit.

system at one of its natural frequencies ($f_{\text{nat}} = 20$ Hz). Time-domain evolution of the external torque T_{ext} [see Fig. 5(a)] as well as torque on the shaft T_{shaft} [see Fig. 5(b)] is presented. The results are obtained from a rotor shaft system of a three-phase, two-pole, squirrel cage induction-type electric motor rated 6.6 kV, which is widely used in ESP applications [27]. The following equation provides the characteristics of external applied torque T_{ext}:

$$\begin{cases} T_{\text{ext}} = 5000 + T_1 sin\,(2\pi \cdot 20t)\, N \cdot m \\ T_1 = 0N \cdot m\ if\ t < 3.5s \\ T_1 = 500N \cdot m\ if\ t \geq 3.5s. \end{cases} \tag{8}$$

These values are illustrative only and represent the instantaneous torque components in the motor shaft. According to (8), T_{ext} is obtained from a dc torque of 5 kN·m added to a torque component oscillating with a frequency of 20 Hz and a magnitude of 500 N·m (i.e., 10% of dc torque). In Fig. 5(b), it can be observed that at $t = 3.5$ s, the resultant torque on the shaft is linearly increasing with time because 20 Hz is also the natural frequency of the shaft. The torque on the shaft will be increasing over time, which might induce accelerated fatigue or shaft breakdown. This conclusion can be extended to a more complex rotating shaft system having multi-inertia, where the number of natural frequencies is dependent on the number of inertias. In VFD-ESP systems, VFD provides voltage and current harmonics such that when combined in the motor air gap, they generate unwanted torque components that might coincide with shaft torsional natural frequencies, potentially leading to mechanical-shaft failures [28]. Consequently, VFDs should be designed to provide torque components with substantially low magnitude at specific frequencies to avoid the resonance excitation of the shaft. Besides the VFD-induced resonance excitation, there are also other possible sources that may excite the resonance modes of a given ESP shaft. They include mechanical induced sources such as shaft misalignment and mechanical component failure such as bearing [29]. Finally, process-induced sources such as hydrocarbon fluid velocity, gas slug, and sand may also excite the eigenmodes of the ESP shaft [30].

2) Generalized Model of Multi-Inertia Shaft Systems: Because most of the mechanical shafts are multi-inertia systems, it is necessary to represent their model for any system integration analysis. A generic representation of a multi-inertia shaft system is shown in Fig. 6(a), where the shaft is divided into $(x-1)$ branches. At a given node, the elements of the shaft consist of a set of mass moments of inertia denoted $J_1, \ldots, J_x$. They are coupled at each adjacent node by shaft elements with stiffness constants $k_{12}, \ldots, k_{(x-1)x}$ and with damping coefficients $d_{12}, \ldots, d_{(x-1)x}$ and $d_{10}, \ldots, d_{S0}$. Each node *j* has only a single degree of freedom θ_j. In this representation, the motor inertia is denoted J_x. According to [31], a rotating shaft system can be analyzed in a similar way as a simple *RLC* circuit, and the system equation of motion is based on Newton's second law. With such an approach, moments of inertia are equivalent to inductances, damping factors to resistances, and inverse stiffness constants to capacitances. Mechanical quantities also have their equivalent electrical quantities: angular velocity is equivalent to current, and torque to voltage. Fig. 6(b) shows the phenomenological equivalent electrical circuit of a mechanical shaft system. As illustrated, all motor air gap torque components feed the electrical system as a controlled voltage source near the motor inertia. Process-induced vibrations such as gas slugs are converted to mechanical torque components and are feeding the circuit as a controlled voltage source near the first inertia for the sake of simplicity. Normally, process-induced torque should supply the circuit at each branch. Newton's second law applied to the shaft system illustrated in Fig. 6 is a differential equation

$$\boldsymbol{J}\frac{d\theta^2\,(t)}{dt^2} + \boldsymbol{D}\frac{d\theta}{dt} + \boldsymbol{K}\,\theta\, = \boldsymbol{T}_{\text{ext}} \tag{9}$$

where $\boldsymbol{J}$ is the matrix of mass moment of inertia, $\boldsymbol{D}$ is the damping coefficient matrix, $\boldsymbol{K}$ is the stiffness matrix, and $\boldsymbol{T}_{\text{ext}}$ is the matrix of externally applied torque to the shaft system, and elements of these matrices are calculated in [31].

The natural frequencies $\omega_{\text{nat},i}$ of the shaft system are calculated as the square root of the solutions of the following

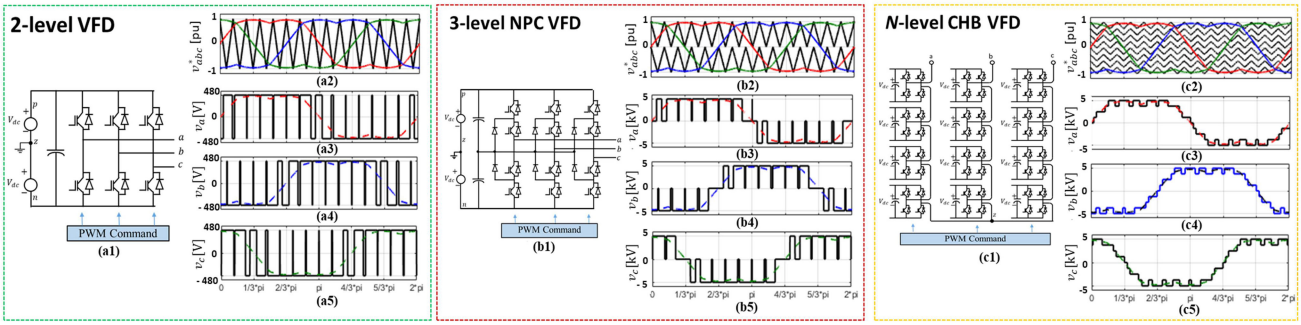

Fig. 7. Investigated VFD topologies and their corresponding switching function waveforms. (a) Two-level VFD. (b) Three-level NPC VFD. (c) *N*-level CHB VFD.

characteristic equation:

$$\left[\boldsymbol{J}^{-1}\boldsymbol{K} - \lambda \boldsymbol{I}\right] = 0 \tag{10a}$$

$$\omega_{\mathrm{nat},i}^2 = \lambda_i \,, i = 1,\ 2,\ \ldots, x \tag{10b}$$

where $\boldsymbol{I}$ is the identity matrix and λ_i are the roots of (9). This modeling approach can be easily transformed into a state-space form, which is suitable for control purposes as well as for the dynamic analysis of the shaft system. State variables can, therefore, be chosen such that shaft disturbances can be understood, their impact on the electrical system assessed, and the control of VFD can be tuned.

III. Proposed Simplified VFD-ESP Model for Output PQ Analysis

A. Preliminary Considerations

The overall equivalent model of the system introduced in Fig. 2 is developed in this section. The purpose of this model is to analyze the PQ of an integrated VFD-ESP system. This analysis is performed through a detailed understanding of three state variables: the VFD output voltage, the motor current, and the electromagnetic air gap torque. The investigated system is, therefore, a coupled electrical and mechanical system, even though it has been represented with electrical components only. The cable model has multiple inductances and capacitors; therefore, it is considered a high-inertia system according to the electromechanical analogy [31]. The dynamics of the electrical system (the VFD only) is faster compared with the dynamics of the cable and much faster compared with the dynamics of the mechanical system. Because the control of the VFD influences only the dynamic of the VFD itself, it has a minor influence on the dynamic of the remaining system with slow dynamics. Consequently, the system is analyzed in steady state only, which, therefore, leads to a simplified model of the ESP for PQ analysis. Finally, it is reasonable to assume that VFDs only operate with a constant voltage per hertz (*V/f*) open-loop control providing the pulsewidth modulation (PWM) reference voltage setpoint according to a desired ESP motor speed or frequency.

Fig. 7 shows the industrial preferred voltage source inverter topologies used in ESP applications with their corresponding output switched waveforms. They are, respectively: 1) LV two-level inverter [see Fig. 7(a)]; 2) three-level NPC inverter [see Fig. 7(b)]; and 3) N -level CHB [see Fig. 7(c)] [25]. The input supply is not shown because it has a negligible impact on the output spectrum of the VFD voltage due to a substantially large dc-link capacitor in these topologies. To replicate the output voltage behavior of a VFD topology, computer tools are classically used, where the full PWM strategy and VFD power stage, including power switches (e.g., IGBTs), are implemented [21]–[23]. The preferred modulation strategy is the sine-triangle PWM technique, and the phase-disposition (PD) PWM approach is widely used for multilevel VFD topologies because it provides reduced voltage and current total harmonic distortion [32]. A "Decoding and Gating unit" is often used to translate the result of the sine-triangle comparison to appropriate gating signals [32]. Implementing such an approach for multilevel VFD topologies can be troublesome for field engineers, and the internal behavior of a specific VFD is manufacturer dependent. To avoid such a task, a simple approach to mimic the VFD output voltage without understanding its internal behavior is proposed in Section III-B.

B. Simplified VFD Simulation Model

The proposed model is based on a switching function representation suitable for steady-state analysis. With this approach, the "Decoding and Gating unit" described in Section III-A and the power stage are replaced by a model that only takes into account the "PWM Generation unit" and the dc-link voltage. Specific examples of this suggested technique are shown in Fig. 8, which shows the results for its application to a two-level converter [see Fig. 8(a)], a three-level three-NPC converter [see Fig. 8(b)], and to an N -level CHB converter [see Fig. 8(c)]. To build the simplified VFD switching model, a per-phase reference sine wave v_i^* $(i \in \{a,\ b,\ c\})$ is compared with phase-shifted or level-shifted triangle carriers to obtain individual sub-PWM signals $S_{ij} \in \{0,\ 1\}$. Then, all sub-PWM signals are added to produce the desired switched PWM signal. A negative offset equal to $(N-1)/2$ is used to map the comparison results to the voltage levels in per unit with respect to the dc-link voltage. For a two-level VFD, V_{dc} is the total dc-link voltage. For a three-level VFD, only half of the total dc-link voltage is used, and for an *N*-level model, V_{dc} is the dc-link voltage of one power cell. An

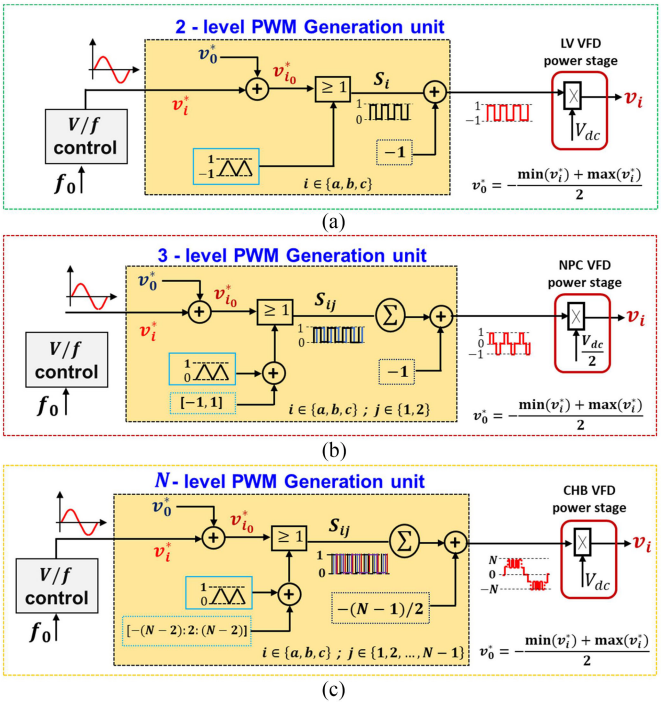

Fig. 8. Proposed VFD switching models. (a) Two-level VFD model. (b) Three-level NPC VFD model. (c) Multilevel CHB VFD model.

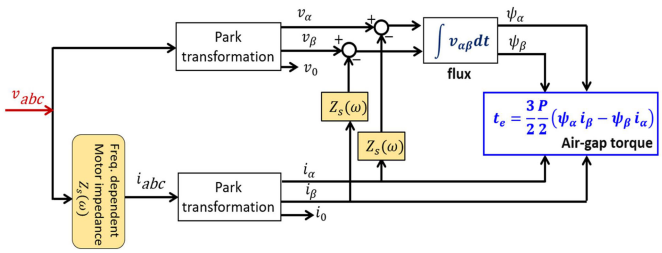

Fig. 9. Air gap torque model for mechanical resonance analysis.

average between the minimum and the maximum values of the three-phase references is used as a homopolar component v_0^*, which is injected into each reference phase voltage v_i^* to mimic the behavior of the space-vector controlled VFD. The space vector modulation is known to produce up to 15% more voltage than the PWM technique without a homopolar component [33]. Once these models are defined, the configuration of the VFD power part is not needed anymore for the overall system analysis.

C. General Motor Electromagnetic Torque Model

For a P-pole electrical machine (induction or synchronous) driven by a VFD, the electromagnetic torque $t_e(t)$ is to be taken as the output of the model, whereas the voltages and currents are the inputs for the sake of simplicity. Fig. 9 shows a simple approach to reconstruct the torque dynamic behavior in the ESP motor air gap. This model only uses the measured three-phase stator voltages and currents, thus avoiding the use of torque sensors. Such an approach is consistent with practical applications, where direct measurement of air gap torque is generally not possible. As illustrated, the air gap torque is created by a combination of electromagnetic flux and current. The electrical quantities are expressed in the $\alpha\beta$, the stationary orthogonal reference frame, in order to properly capture the effects of frequency superposition in the air gap. The flux is approximated as the time integral of the voltage. The voltage drops resulting from the stator impedance can be neglected because the stator impedance does not influence the location of torque components in the frequency domain; it only slightly modifies their magnitudes [34]. This model does not consider the air gap torque resulting from the process dynamic load. From a purely mathematical point of view, dynamically induced process mechanical torque components are simply added to the electromagnetic torque produced by the electrical harmonics.

D. Proposed Simplified VFD-ESP Model Description

Fig. 10 shows the block diagram of the proposed simplified VFD-ESP model. The model is suitable for coupled electrical and mechanical resonance analysis in steady state. On the left side of the scheme, the VFD model is introduced, and it is represented as a PWM switching function multiplied by the dc-link voltage, as described in Section III-B. This voltage is applied at the cable model sending end. The cable is represented as a lumped element model with multiple pi-sections (for example, one pi-section per kilometer). In addition, skin effects and all reflection points, such as cable splices, penetrators, and connectors, are ignored in this transmission system model as their effects are negligible per system design requirements. The voltage at the receiving end of the cable model is then applied to the motor air gap model (blue-dashed block), which is computed as the interaction between stator flux and current in $\alpha\beta$ coordinates. On the right side of the scheme, the model of the shaft system is shown as a multi-inertia system through the electromechanical analogy, as described in Section II-B. Process-induced mechanical torque components, such as gas slugs, are supplied to the shaft model as an externally controlled voltage source. These torque components may induce current pulsations flowing from the motor windings back to the VFD [34]. The air gap torque model is inserted between the electrical and mechanical subsystems such that it becomes easy to emulate the reversible propagation of electrical and mechanical harmonics.

IV. Analytical Expressions of Different Types of Harmonics in VFD-ESP Systems

A. Electrical Harmonics

1) VFD Output Harmonic Families: The analytical expression of the switching function of any PWM strategy applied to any VFD power topology can be obtained from a double Fourier transformation and be written as follows [35]:

$$S_{a\mathrm{VFD}} = \sum_{m=0}^{\infty} \sum_{n=-\infty}^{\infty} S_{m,n} \cos\left(m\omega_c t + n\omega_0 t + \theta_{m,n}^{v}\right) \tag{11a}$$

$$v_{a\mathrm{VFD}}\ (t) = S_{a\mathrm{VFD}}\ (t) * V_{\mathrm{dc}} \tag{11b}$$

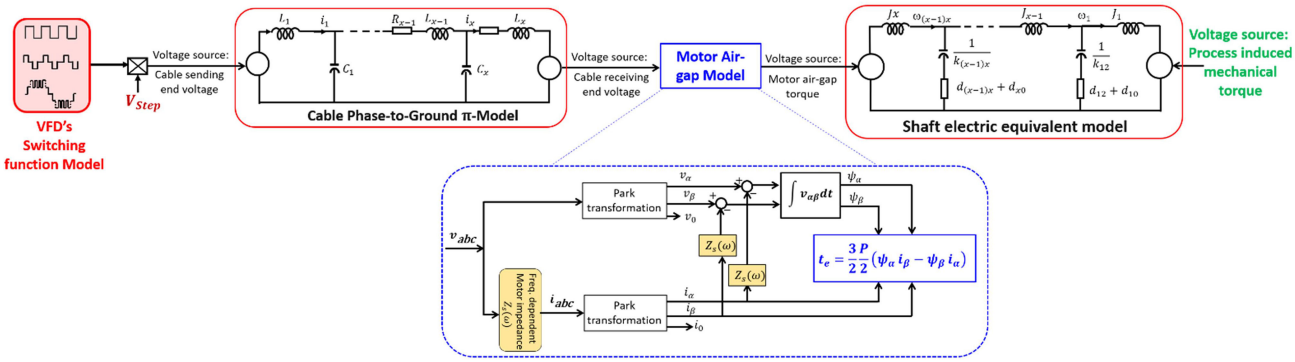

Fig. 10. Proposed simplified VFD-ESP model for coupled electrical and mechanical resonance analysis.

TABLE I
HARMONIC FAMILIES AT THE OUTPUT OF THE TWO-LEVEL, THREE-LEVEL, AND *N*-LEVEL VFDS

VFD type / Harmonic families	2-level	3-level NPC	*N*-level CHB
DC-component	1		
Fundamental	$M\cos(\omega_0 t)$	$S_{0,1}\cos(\omega_0 t)$	$\frac{N-1}{2}S_{0,1}\cos(\omega_0 t)$
Baseband		$\sum_{n=2}^{\infty} S_{0,2n-1}\cos\big((2n-1)\omega_0 t\big)$	$\frac{N-1}{2}\sum_{n=2}^{\infty} S_{0,2n-1}\cos\big((2n-1)\omega_0 t\big)$
Carrierband		$\sum_{m=1}^{\infty} S_{2m,0}\cos(2m\omega_c t)$	$\frac{N-1}{2}\sum_{m=1}^{\infty} S_{(2m-1),0}\cos\big((2m-1)\omega_c t\big)$
Sideband	$\frac{4}{\pi}\sum_{m=1}^{\infty}\sum_{n=-\infty}^{\infty} S_{m,n}\cos\,(m\omega_c t + m\omega_0 t)$	$\sum_{m=1}^{\infty}\sum_{n=-\infty}^{\infty} S_{(2m-1),2n}\cos\begin{bmatrix}(2m-1)\omega_c t \\ +2n\omega_0 t\end{bmatrix}$ $+\sum_{m=1}^{\infty}\sum_{n=-\infty}^{\infty} S_{2m,2n+1}\cos\begin{bmatrix}2m\omega_c t + \\ (2n+1)\omega_0 t\end{bmatrix}$	$\sum_{m=1}^{\infty}\sum_{\substack{n=-\infty \\ n\neq 0}}^{\infty} S_{(2m-1),2n}\cos\begin{bmatrix}2(m-1)\omega_c t \\ +2n\omega_0 t\end{bmatrix}$ $+\sum_{m=1}^{\infty}\sum_{n=-\infty}^{\infty} S_{2m,2n+1}\cos\begin{bmatrix}(2m\omega_c t + \\ (2n+1)\omega_0 t\end{bmatrix}$

where ω_c and ω_0 are, respectively, the PWM triangle carrier and the fundamental frequencies; and $\theta^{v}_{m,n}$ is the voltage harmonic phase shift with respect to the fundamental PWM strategy being used. The switching function is multiplied by the voltage step $V_{\rm dc}$, as shown in (11b). Equation (11) is given for phase *a*, and it is horizontally shifted by $\pm 2\pi/3$ for phases *b* and *c*. The set of integers (m, n) can be selected depending on the type of PWM strategy being considered. The theoretical harmonic families at the output of the two-level, three-level, and N -level VFDs are summarized in Table I. Depending on the values of $(m,\ n)$, the following types of electrical harmonics can be derived [35]:

1) if $m = 0$ and $m = 0$, dc component;
2) if $m = 0$ and $n = 1$: fundamental voltage component;
3) if $m = 0$ and $n > 1$: baseband voltage harmonics, only positive and negative sequence components are visible, i.e., $n = |6l \pm 1|$, $l = 0,\ 1,\ 2,\ \ldots$;
4) if $m \neq 0$ and $n \neq 0$: sideband voltage harmonics, particularly for the case of NPC and CHB VFDs, visible sideband carrier harmonics are the ones where even values of m are paired with odd values of n and vice versa, as shown in

$$m = 2,\ 4,\ 6,\ \ldots,\ n = 0 \pm 1,\ \pm 3,\ \pm 5,\ldots \quad (12a)$$

$$m = 1,\ 3,\ 5,\ldots,\ n = \pm 2,\ \pm 4 \pm 6,\ldots. \quad (12b)$$

2) Notes on Sideband or Interharmonics: Sideband or interharmonics are sometimes misinterpreted, as discussed in the sequel. Even if most of the existing papers devoted to harmonics represent harmonic frequencies in the form of a rank with respect to the fundamental frequency [36], only baseband harmonics are expressed in these papers. This misinterpretation leads to a wrong understanding of VFD-induced harmonic locations in the frequency domain. As an example, assume a PWM frequency $f_c = 750$ Hz and an ESP motor supplied by a VFD running at a fundamental frequency $f_0 = 50$ Hz. A harmonic located at 350 Hz coincides with the 7th harmonic $f_{07} = 7 \times 50$ Hz , but it can also coincide with a sideband harmonic $f_{18} = |750 - 8 \times 50|$ Hz, where $(m, n) = (1,\ 8)$. If the motor speed is reduced such that $f_0 = 40$ Hz , then the 7th harmonic becomes: $f_{07} = 7 \times 40$ Hz $= 280$ Hz , while the sideband harmonic becomes: $f_{18} = |750 - 8 \times 40|$ Hz $= 430$ Hz , which might wrongly be approximated to $\frac{430}{40} = 10.75$ Hz $\approx$ 11th harmonic. Any changes in the PWM frequency will also produce a different result. This example explains why a clear understanding of modulation switching functions is important

for PQ analysis with VFDs. It provides a theoretical root of most harmonics and an in-depth understanding of some unexplained or random behaviors of VFDs.

3) Notes on Common-Mode Voltage Harmonics From VFDs: Common-mode voltage harmonics are components that are present in all phases. They are seen in phase-to-ground paths or to any common reference point through an impedance (phase-to-ground or leakage impedance). From a mathematical point of view, a common-mode component $\boldsymbol{v_{\mathbf{com}k}}\ (\boldsymbol{t})$ is the one that has the same phase shift in all the three phases such that

$$v_{\mathrm{com}k}\ (t) = V_{\mathrm{com}_k}\ \cos\left(\lambda\omega_k t + \phi_k\right) \tag{13a}$$

$$v_{a_k}\ (t) = v_{b_k}\ \ (t) = v_{c_k}\ (t) \tag{13b}$$

where k and λ are the arbitrary integers, ω_k is an arbitrary frequency, ϕ_k is an arbitrary phase shift, and V_{com_k} is the magnitude of the common-mode harmonic component. v_{a_k}, v_{b_k}, and v_{c_k} are the harmonics of phases *a, b,* and *c*, respectively. In three-phase systems, all baseband triplen harmonics are common-mode quantities [33].

According to Table I, it can be noticed that the modulation process inherently creates common-mode voltage harmonic components for all investigated VFD architectures. Thus, all carrier-band harmonics are, therefore, common-mode components and are, respectively, given in (14)–(16) for all the investigated VFDs

$$\mathrm{V}_{\mathrm{com}_{\mathrm{LV}}}\ (t) = V_{\mathrm{dc}}\ + V_{\mathrm{dc}} \sum_{m\,=\,1}^{\infty} S_{m,0} \cos\left(m\omega_c t\right) \tag{14}$$

$$V_{\mathrm{com}_{\mathrm{NPC}}}\ (t) = V_{\mathrm{dc}}\ \sum_{m\,=\,1}^{\infty} S_{2m,0} \cos\left(2m\omega_c t\right) \tag{15}$$

$$V_{\mathrm{com}_{\mathrm{CHB}}}\ (t) = V_{\mathrm{dc}}\ \sum_{m\,=\,1}^{\infty} S_{(2m-1),0} \cos\left((2m-1)\,\omega_c t\right). \tag{16}$$

These components do not produce any energy to be transferred to the load because they are canceled through the differentiation of the phase-to-phase voltages. In addition, they are not seen by any sine filter, which usually acts on differential-mode components only.

B. Electromagnetic Torque Harmonics

Equation (17) is a generic motor electromagnetic instantaneous torque equation induced by any VFD with all harmonic families. It includes the dc component, baseband, and sideband harmonic families, where $T_{e,m,n}$ and $\theta^{Te}_{m,n}$ are, respectively, the torque harmonic magnitude and phase.

$$t_e\ (t) = \sum_{m=0}^{\infty} \sum_{n=-\infty}^{\infty} T_{e,m,n} \cos\left(m\omega_c t + n\omega_0 t + \theta^{Te}_{m,n}\right). \tag{17}$$

The theoretical foundations of this equation are given in [37]. Depending on the type of VFD and its command strategy, torque harmonic components with relevant magnitudes can be derived by selecting appropriate $(m,\ n)$ parameters. Thus, all the relevant harmonic components of motor air gap torque when supplied by two-level, three-level NPC, multilevel CHB VFD topologies are given in (18)–(20), respectively

$$t_{e\mathrm{LV}}\ (t) = T_{\mathrm{DC}}\ + \sum_{l\,=\,1}^{\infty} T_{e,0,\,6l} \cos\left(6l\omega_0 t\right) \tag{18a}$$

$$+ \sum_{m\,=\,1}^{\infty} \sum_{\substack{n\ =\ -\infty \\ n\,\neq\,0}}^{\infty} T_{e,m,n} \cos\left(m\omega_c t + n\omega_0 t\right) \tag{18b}$$

$$t_{e\mathrm{NPC}}\ (t) = T_{\mathrm{DC}}\ + \sum_{n\,=\,1}^{\infty} T_{e,0,6n} \cos\left(6n\omega_0 t + \theta_{0,6n}\right) \tag{19a}$$

$$+ \sum_{m\,=\,0}^{\infty} \sum_{n\,=\,0}^{\infty} T_{e,2m,\pm 6n} \cos\left(2m\omega_c t \pm 3\,(2n)\,\omega_0 t\right) \tag{19b}$$

$$+ \sum_{m\,=\,1}^{\infty} \sum_{n\,=\,0}^{\infty} T_{e,2m-1,\pm 3(2n+1)} \cos\left((2m-1)\,\omega_c t \pm 3\,(2n+1)\,\omega_0 t\right). \tag{19c}$$

$$t_{e\mathrm{CHB}}\ (t) = T_{\mathrm{DC}}\ + \sum_{n\,=\,1}^{\infty} T_{e,0,6n} \cos\left(6n\omega_0 t\right) \tag{20a}$$

$$+ \sum_{m\,=\,1}^{\infty} \sum_{n\,=\,-\infty}^{\infty} T_{e,2m,\,\pm 6n} \cos\left(2m\omega_c t \pm 3\,(2n)\,\omega_0 t\right) \tag{20b}$$

$$+ \sum_{m\,=\,1}^{\infty} \sum_{n\,=\,0}^{\infty} T_{e,(2m-1),\pm(2n+1)} \cos\left((2m-1)\,\omega_c t \pm (2n+1)\,\omega_0 t\right). \tag{20c}$$

Torque harmonic phases have been ignored in these expressions for the sake of simplicity. Note that in the theoretical relationships (18)–(20), the torque components resulting from the machine construction irregularities have been neglected; their frequencies are usually proportional to the motor speed. However, for rigorous analysis, they can be taken into account by adjusting the magnitude of the baseband torque components produced by the VFDs. In addition, the analytical model does not consider the air gap torque resulting from the process dynamic load. Each oscillating mechanical torque component $t_{m_j}\ (t) = T_{m_j}\ \cos(\omega_{m_j} t)$ creates two new current harmonics at frequencies $|\omega_{m_j} \pm \omega_0|$ by slightly modifying the rotor speed. These new current components also interact with the fundamental voltage to create new sideband torque components in the air gap to balance the air gap energy.

V. Numerical and Experimental Validations

A. Offline Numerical Validations

1) Simulated System Description and Validation Principle: The proposed VFD-ESP model is implemented and simulated with two-level, three-level NPC, and seven-level CHB inverters in MATLAB/Simulink environment. To verify the effectiveness of the proposed approach, the results obtained with the proposed

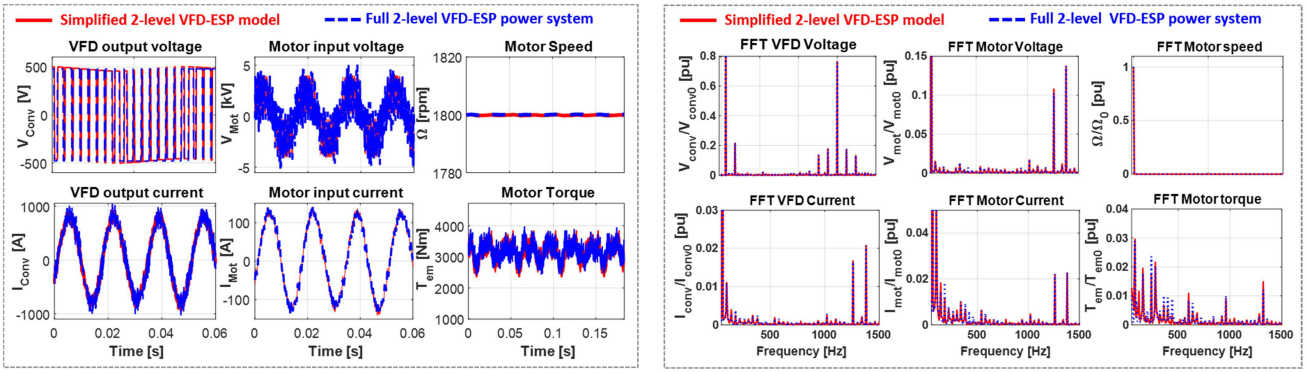

Fig. 11. Sample comparison simulation results between the proposed model and the complete two-level VFD-ESP system both in time and frequency domains at $f_c = 1$ kHz and $f_0 = 60$ Hz. (a) Time domain. (b) Frequency domain.

TABLE II
PARAMETERS OF SIMULATION

Cable	**ESP motor**
Length (km) =1.5	900 HP, 4385 V, 124 A, 60 Hz
Resistance (Ω/km)=0.160	Stator resistance: R_s= 0.034 pu
Inductance (mH/km)=0.34	Stator inductance: L_s= 0.0851 pu
Capacitance (μF/km)=0.379	Rotor resistance: R_r= 0.043 pu
	Rotor inductance: L_r= 5.2 mH
PWM unit	Magnetizing reactance: X_m= 1.92 pu
Carrier frequency:	Inertia J= 22 kgm^2
f_c =1 kHz	Pole pair P = 2
Fundamental frequency	Load torque T_L = 3000 Nm
f_0 = 60 Hz	Nominal speed Ω = 1800 rpm

model are compared with those obtained from the complete ESP system model, in which the VFD power topology, including IGBTs, step-up transformer, transmission cable, and electrical induction machine and its load torque are connected. The complete ESP system model is built in MATLAB, using the SimpowerSystems blockset, where VFDs are built using IGBT components. Also, speed and current controllers with their respective feedback have been implemented to provide the voltage reference to the PWM modulator. A "Decoding and Gating unit" is used to translate the result of the sine-triangle comparison to the IGBT gating signals. The transmission cable model is built using SimpowerSystems components with adequate parameters, with three-pi sections. The induction motor (IM) uses the motor block of the SimpowerSystems toolbox and it is connected to the mechanical components provided by the SimMechanics toolbox.

The proposed VFD-ESP model is implemented according to Fig. 10, where the VFD output voltage is built as the product of the dc-link voltage and the per phase switching function (see Fig. 8). There is no controller, and there are no power devices. The cable model is built with a three-pi section using the investigated cable per length parameters. The steady-state impedance of an IM is supplied by the voltage generated by the simplified VFD model, and the corresponding currents and voltages are Park-transformed to deduce the instantaneous electromagnetic torque of the motor, as shown Fig. 9. The two-inertia mechanical shaft is built with electrical components, as described in Section II-B (see Fig. 6). The parameter of the ESP system components used in the simulation is provided in Table II [4]. Simulations were performed and the following state variables were recorded and postprocessed for visualization and comparison purposes:

1) VFD output voltage and current ($V_{\rm Conv}$, $I_{\rm Conv}$);
2) motor input voltage and current, i.e., cable receiving-end voltages and currents ($V_{\rm Mot}$, $I_{\rm Mot}$);
3) motor speed and torque (Ω , T_{em}).

For the comparison in the frequency domain, a fast Fourier transform (FFT) with 1 Hz resolution and even window length is applied to the recorded time-domain waveforms.

2) Offline Simulation Results and Discussions: Fig. 11 shows sample time-domain [see Fig. 11(a)] and frequency-domain [see Fig. 11(b)] comparison simulation results for an ESP system with a two-level VFD. As it can be observed, there is a good agreement between the results obtained from the proposed simplified model (red straight lines) and the ones obtained from the complete ESP power system (blue dashed lines). Similar simulation comparison results both in time and frequency domains are shown in Figs. 12 and 13, for a three-level NPC and seven-level CHB VFD-ESP system, respectively. Again, it can be noticed that both simulated models provide quite similar waveforms of $\boldsymbol{V}_{\mathbf{Conv}}$, $\boldsymbol{I}_{\mathbf{Conv}}$, $\boldsymbol{V}_{\mathbf{Mot}}$, $\boldsymbol{I}_{\mathbf{Mot}}$, and $\boldsymbol{T}_{\boldsymbol{em}}$ with good achievement of their expected nominal values. The frequency-domain results [see Figs. 11(b), 12(b), and 13(b)] indicate a stronger correlation and good fit between both simulated models by producing similar harmonic components located at the same frequencies.

There is only a slight difference in the magnitude of some harmonic components. An error evaluation of frequency-domain results of VFD output voltage ($V_{\rm Conv}$), motor current ($I_{\rm Mot}$), and torque (T_{em}) for each simulated model is provided in Table III. The mean absolute percentage error (MAPE) is used for this evaluation and is computed as [38]

$$\text{MAPE} = \frac{100}{N_h}\sum_{h=1}^{N_h}\left|\frac{X_h - \overline{X_h}}{X_h}\right| \tag{21}$$

where N_h is the number of harmonic components, X_h is the magnitude of the h th coefficient of the FFT component obtained using the proposed simplified model, and $\overline{X_h}$ is the same as X_h

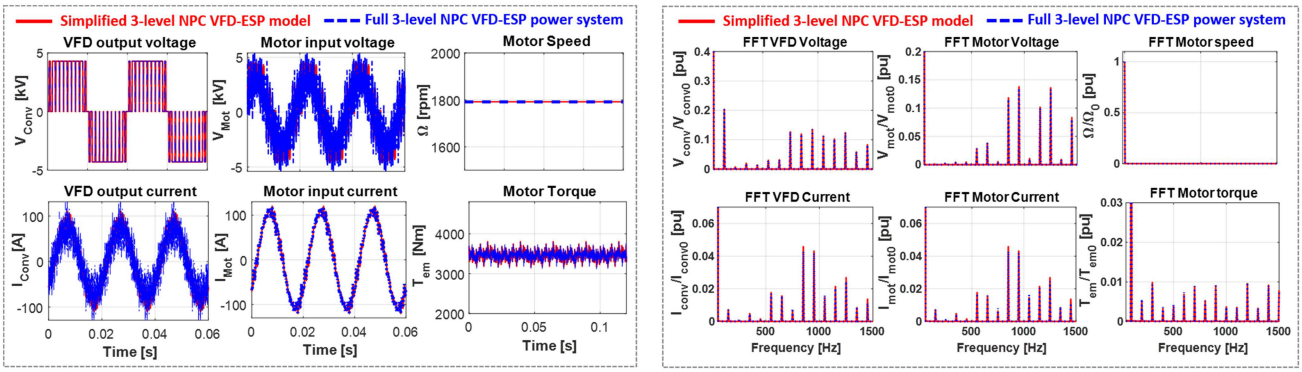

(a) (b)

Fig. 12. Sample comparison simulation results between the proposed model and the complete three-level NPC VFD-ESP system both in time and frequency domains at $f_c = 1$ kHz and $f_0 = 60$ Hz. (a) Time domain. (b) Frequency domain.

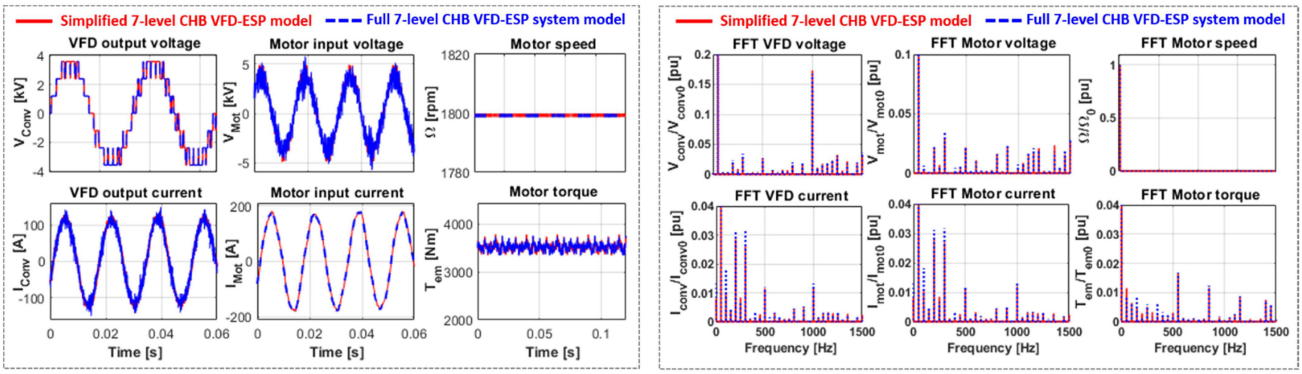

(a) (b)

Fig. 13. Sample comparison simulation results between the proposed model and the complete seven-level CHB VFD-ESP system both in time and frequency domains at $f_c = 1$ kHz and $f_0 = 60$ Hz. (a) Time domain. (b) Frequency domain.

TABLE III
MAPEs BETWEEN THE PROPOSED SIMPLIFIED MODEL AND THE COMPLETE ESP MODEL IN THE FREQUENCY DOMAIN

	MAPE of V_{Conv}(%)	MAPE of I_{Mot}(%)	MAPE of T_{em}(%)
2-Level VFD-ESP	0.04	0.24	5.03
3-Level NPC VFD-ESP	0.30	0.73	9.0
7-Level CHB VFD-ESP	0.01	0.05	1.0

but obtained from the complete ESP system model. According to the results in Table III, it can be noticed that the error of VFD output voltage, motor current, and torque errors in all studied cases are acceptable, which demonstrates a good accuracy between the results obtained from the proposed simplified model and the complete ESP system model. The air gap motor torque errors are slightly higher than the errors obtained for the other variables because the voltage drop caused by stator windings has been neglected when calculating the electromagnetic torque with the proposed approach.

As discussed in Section III-C, the stator impedance does not influence the location of torque components in the frequency domain; it only slightly modifies their magnitudes [34]. Finally, it can be concluded that the proposed model is a simple and accurate computer tool to simulate the steady-state behavior of the ESP systems, regardless of the type of VFD topology involved.

B. *Real-Time Hybrid Numerical Validations*

1) Real-Time Hybrid Validation Procedure: The validity and robustness of the proposed model shown in Fig. 10 are finally verified through real-time hybrid simulations (RTHSs). RTHS is a testing method where a structure of a given power system is divided into physical (real/analogical) and numerical/digital parts, which are then coupled in real time. The idea is to verify if the proposed model is designed such that it can mimic as close as possible the overall behavior of a given VFD-ESP system using the field data measurements of a part of that system. For illustrative purposes, Fig. 14 shows the output voltage test results obtained from the NPC [see Fig. 14(a)] and CHB [see Fig. 14(b)] converters. These results are obtained from a reduced-scale experimental system shown in Fig. 19(b). A detailed description of this experimental setup is provided in Section V-C. RTHS is performed by applying the collected test voltage data at the input

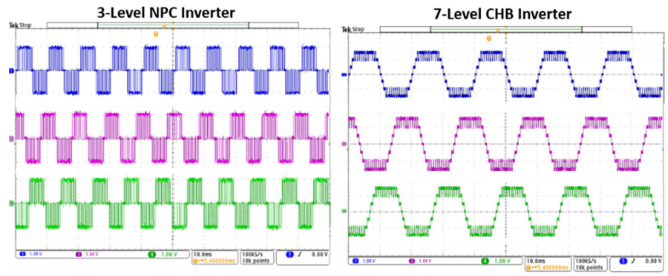

Fig. 14. Output voltage test results of different converters. (a) Three-level NPC inverter. (b) Seven-level CHB inverter.

of the proposed model and running the simulation in real time. Finally, state variables are captured and stored in the MATLAB workspace, then postprocessed for visualization and analysis both in time and frequency domains.

2) RTHS Results and Discussions: The following two field scenarios are considered and discussed, where it is assumed that each investigated VFD-ESP system is operating with different VFD carrier frequency and cable length values:

1) *Case 1: carrier frequency = 1* kHz*; cable length = 1.5* km.
2) *Case 2: carrier frequency = 1.5* kHz*; cable length = 3* km.

To further verify the effectiveness and good performance of the proposed simplified VFD-ESP system model even with real system components involved, comparisons were made between the RTHS results and offline MATLAB-based simulation results obtained with a complete ESP system model. Comparison results between RTHS (black lines) and offline simulations (red lines) of three-level NPC VFD-ESP system for *case 1* are shown in Fig. 15, where the results in the time domain (top part of figures) and frequency domain (bottom part of figures) of VFD output voltage [see Fig. 15(a)], VFD output current [see Fig. 15(b)], motor input voltage [see Fig. 15(c)], motor input current [see Fig. 15(d)], and motor torque [see Fig. 15(e)] are depicted. Fig. 16 shows the comparison results of the three-level NPC VFD-ESP system for *case 2*. Similar comparison results obtained with a seven-level CHB VFD-ESP system for *case 1* and *case 2* are depicted in Figs. 17 and 18, respectively. It can be observed that RTHS results are in close agreement with offline simulation results in all studied cases. Close-form waveshapes of VFD output voltage, VFD output current, motor input voltage, motor input voltage, and motor torque are obtained in all time-domain results. Obviously, there are perceptible disagreements between the waveforms obtained using RTHSs and offline simulations that arise due to the nonideal characteristic of the voltage collected from the real power converters and applied at the input of the proposed model during the RTHSs. These discrepancies do not present a significant impact on the location of harmonics in the frequency domain, as it can be observed from the bottom parts of Figs. 16–19. As illustrated, spectra provided by both RTHSs and offline simulations match quite closely in all the investigated cases. All relevant harmonic components are located at similar frequencies; only their magnitudes do not match exactly. This positive correlation depicts the suitability of the proposed model for the purpose of operational testing with a real system component involved.

Such an approach is consistent with practical applications to closely evaluate the propagation of VFD generated voltage harmonics along the transmission cable and then their impact on the ESP motor can be assessed.

C. Experimental Validation

1) Experimental Setup Description: To demonstrate the accuracy of the proposed model, a down-scale laboratory prototype is built and tested to evaluate the model accuracy. The single-line diagram of the experimental setup is shown in Fig. 19(a) and a picture of the final assembly is depicted in Fig. 19(b) [37]. The overall experimental system includes the following.

1) The VFD under test, which is a seven-level CHB topology with each H-bridge power module based on a Semikron module SK10GD12T4ET rated at 1200 V, 15 A [25]. Each power module has a dc-link voltage rectified from a low-frequency individual transformer.
2) A 10 ft (3 m) electric cable that connects the VFD to the driving machine under test. This is a limitation of the tested system because the length of the transmission cable in a real ESP application is considerably longer than the one used.
3) The machine under test, which is a three-phase 380 V, 3 kW, four-pole IM with 1430 r/min rated speed.
4) A 380 V, 3 kW, eight-pole permanent magnet (PM) generator, supplying a 3 kW dc resistive load through a six-pulse diode bridge rectifier, used as load.
5) An NI-PCI 6229 board that redirects the multitude of command signals to the respective gate drives and acquires the measurement signals [39].
6) A MATLAB/Simulink real-time target machine for programming the controller.
7) Three voltage and three current sensors on both IM and PM sides. A speed sensor is mounted on the IM shaft side, but there is no torque sensor. The instantaneous electromagnetic torque signals in the airgap of both machines are reconstructed based on the principle shown in Fig. 9.

The modulation and control strategies (speed and current control loops) are implemented using the field-oriented control structure, and the parameters of proportional–integral regulators are tuned to accommodate the system setup.

2) Validation Principle and Result Discussions: Fig. 20 shows sample test results for a given operating point with a fundamental frequency of 25 Hz (750 r/min) and two carrier frequencies: 625 and 1200 Hz. The experimental data were collected and plotted using MATLAB for increased clarity and grouped for comparison with simulated results obtained using the proposed model. Fig. 20(a) shows the time-domain test results with a carrier frequency of 625 Hz measured on the driving machine side (IM) [see Fig. 20(a1)–(a3)] and on the PM generator side [see Fig. 20(a4)–(a6)]. Similarly, Fig. 20(b) shows the recorded test results with the PWM carrier frequency of 1200 Hz. In each figure, the voltage, current, and torque

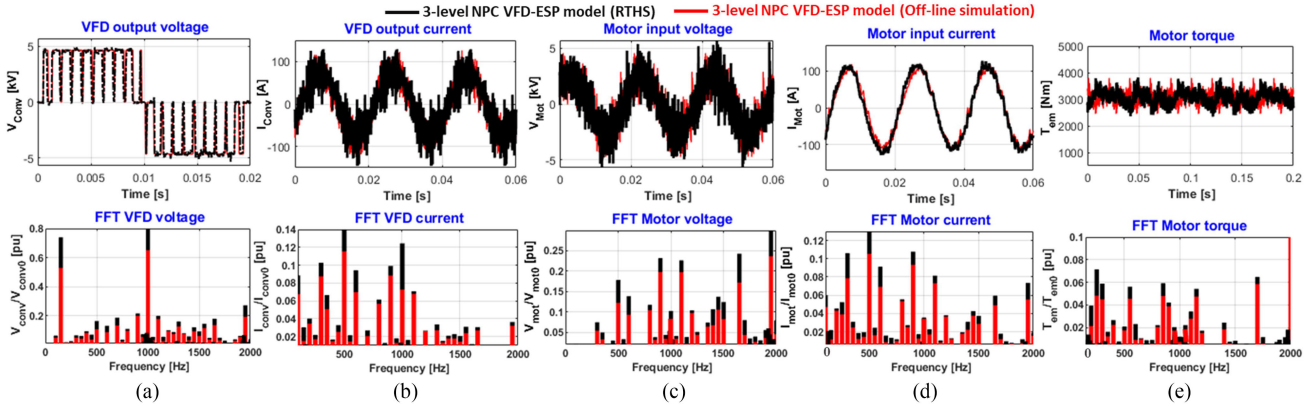

Fig. 15. Time- and frequency-domain comparison results between RTHS and offline simulation for the three-level NPC VFD-ESP system in *case 1*. (a) VFD output voltage. (b) VFD output current. (c) Motor input voltage. (d) Motor input current. (e) Motor torque.

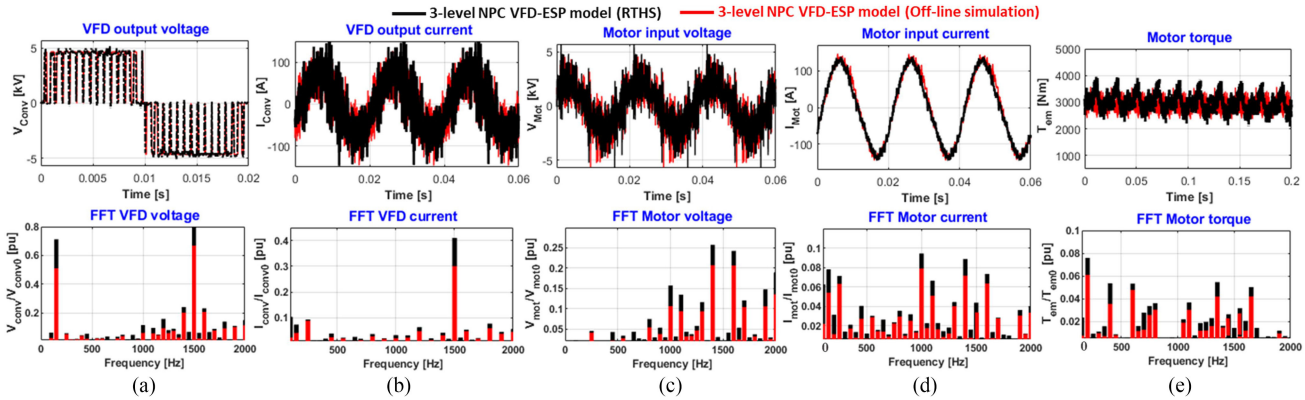

Fig. 16. Time- and frequency-domain comparison results between RTHS and offline simulation for the three-level NPC VFD-ESP system in *case 2*. (a) VFD output voltage. (b) VFD output current. (c) Motor input voltage. (d) Motor input current. (e) Motor torque.

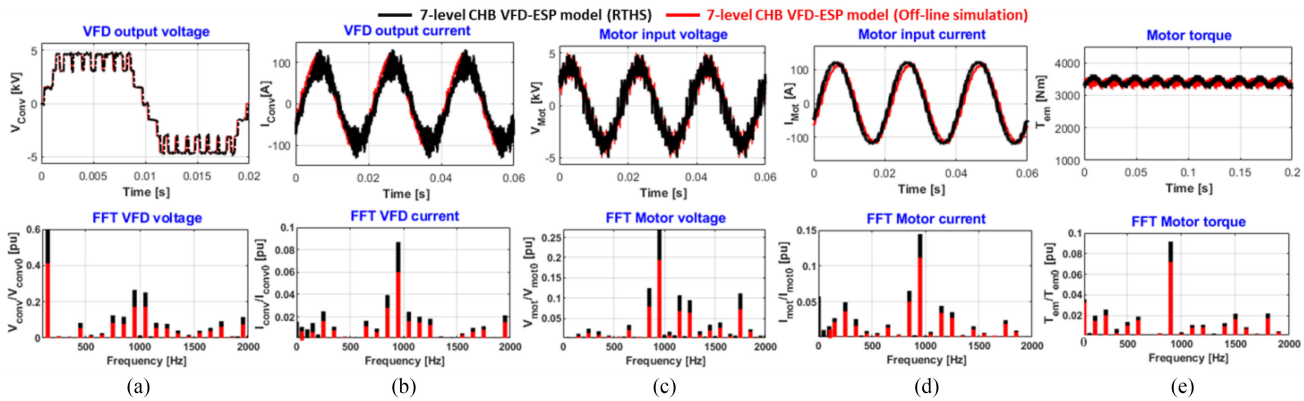

Fig. 17. Time- and frequency-domain comparison results between RTHS and offline simulation for the seven-level CHB VFD-ESP system in *case 1*. (a) VFD output voltage. (b) VFD output current. (c) Motor input voltage. (d) Motor input current. (e) Motor torque.

waveforms on IM and PM sides are depicted. To validate the theoretical approach developed in Section III, experimental results shown in Fig. 21(a)–(b) are compared with the simulated results obtained using the proposed model [see Fig. 10]. The driving-side VFD of the experimental system has been modeled and simulated under the same operating conditions for this validation. Time-domain comparison results for a system operation with $f_c = 625$ Hz and $f_0 = 25$ Hz are shown in Fig. 21(a), where the IM voltage [see Fig. 21(a1)], current [see Fig. 21(a2)], and air gap torque [see Fig. 21(a3)] waveforms are presented. Their amplitudes and frequencies are compared in Fig. 21(b1)–(b3), respectively. Similar comparison waveforms and spectra for the system operation at $f_c = 1200$ Hz and $f_0 = 25$ Hz are shown in Fig. 21(c) and (d). In all the time-domain results, the waveshapes obtained by the simulations using the proposed model and those measured in the experimental setup have shown

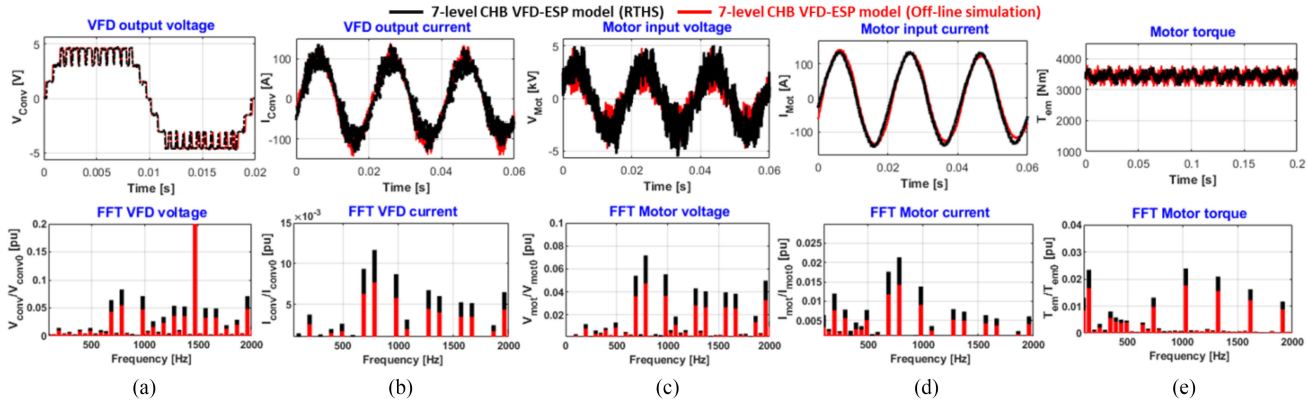

Fig. 18. Time- and frequency-domain comparison results between RTHS and offline simulation for the seven-level CHB VFD-ESP system in *case 2*. (a) VFD output voltage. (b) VFD output current. (c) Motor input voltage. (d) Motor input current. (e) Motor torque.

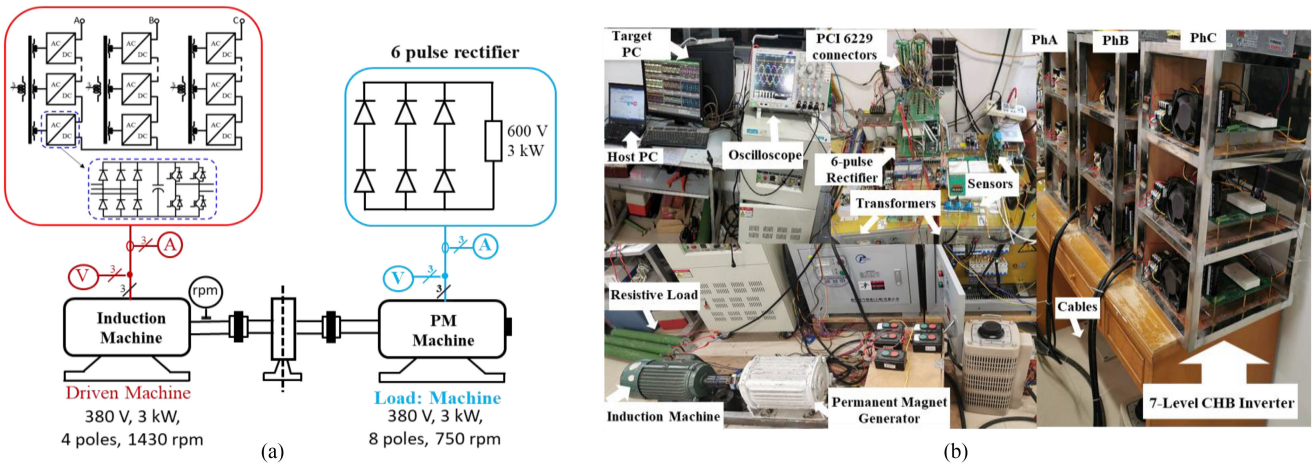

Fig. 19. Down-scale laboratory prototype. (a) Single-line diagram tested system. (b) Picture with key components.

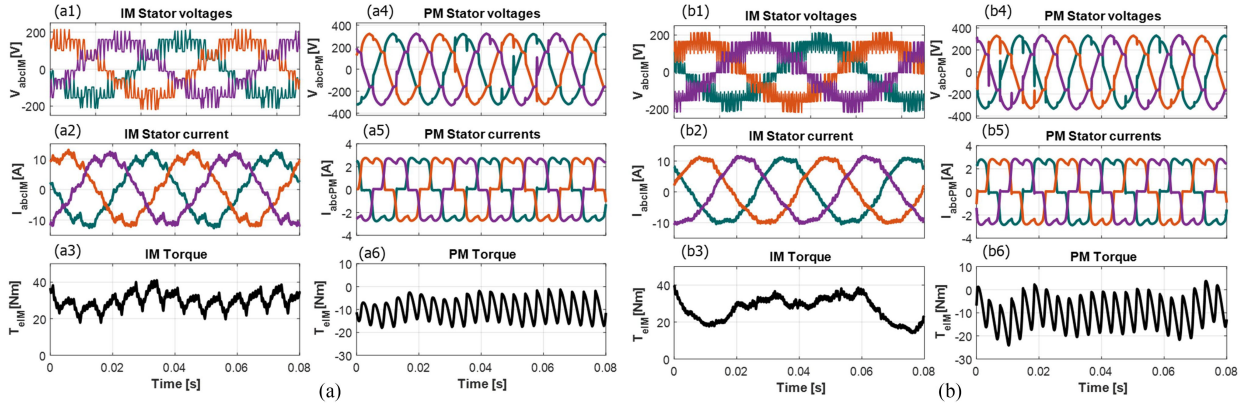

Fig. 20. Sample test results collected at IM and PM sides for different PWM carrier frequencies. (a) $f_c = 625$ Hz. (b) $f_c = 1200$ Hz.

good correlation. The comparison of these waveforms indicates that good representations of the IM voltage, current, and torque behaviors have been achieved in steady state. More importantly, from the examination of Fig. 21(c) and (d), it can be observed that the proposed model yielded frequency-domain simulation results which closely matched the spectra from experimental data. All the dominant harmonic components of measured and simulated spectra of IM voltage [see Fig. 21(c1)–(d1)], current [see Fig. 21(c2)–(d2)], and torque [see Fig. 21(c3)–(d3)] are located at similar frequencies.

The MAPEs between experimental and simulation results in the frequency-domain of the IM voltage (V_{abcIM}), current (I_{abcIM}), and torque (T_{eIM}) are provided in Table IV. As shown in this table, the MAPEs in all investigated cases are less

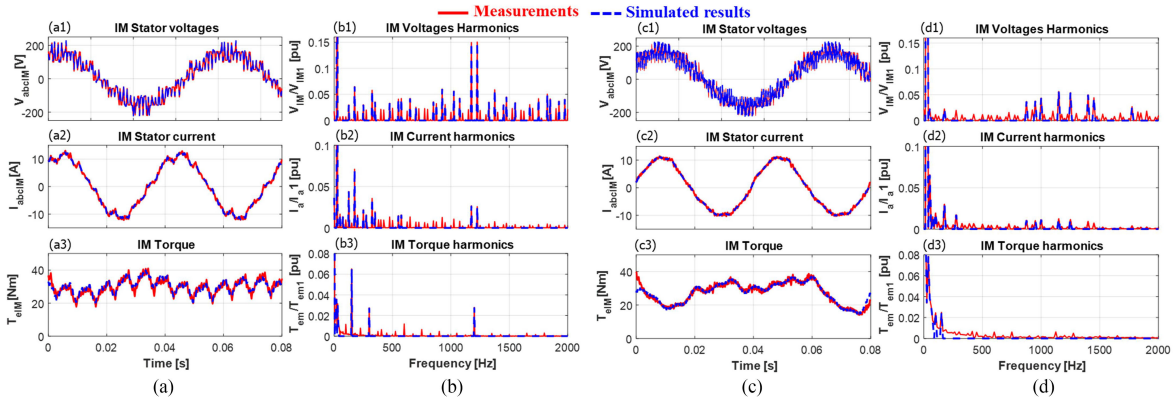

Fig. 21. Time- and frequency-domain comparisons between measured and simulated results. (a) Time-domain results at $f_c = 625$ Hz. (b) Frequency-domain results at $f_c = 625$ Hz. (c) Time-domain results at $f_c = 1200$ Hz. (d) Frequency-domain results at $f_c = 1200$ Hz.

TABLE IV
MAPEs Between Experimental and Simulation Results in the Frequency Domain

	MAPE of V_{abcIM}(%)	MAPE of I_{abcIM}(%)	MAPE of T_{emIM}(%)
7-Level CHB at $f_c = 625$ Hz	0.11	0.06	0.06
7-Level CHB at $f_c = 1200$ Hz	0.26	0.08	0.11

than 1%. This validates the accuracy of the proposed model and confirms that this model can be used with confidence to simulate the steady-state behavior of a VFD-ESP system before it is modified or installed, thus providing a set of possibilities at the design stage to predict possible operating points where risks of electrical and mechanical resonance modes are located. However, the proposed model is not able to replicate harmonics with very small magnitudes, even with the short cable, as found in the experimental system. It is anticipated that the inductive effects of a long cable combined with the skin effects of the cable will lead to highly damped harmonics being reconstructed at the motor terminal, mainly for ESP systems driven by low-power motors (e.g., 30 HP to 50 HP [40]). For higher power applications (e.g., 1500 HP [40]), the behavior of VFD generated voltage and current harmonics will still be restituted at the motor terminals as demonstrated by the offline and hybrid numerical results in this article.

VI. Conclusion

This article proposes a simple modeling approach to easily investigate VFD PQ issues in ESP systems supplied through a long transmission cable. A simplified VFD-ESP model suitable for coupled electrical and mechanical resonance analysis in steady-state is developed in all their configurations of practical interest. It is an easy-to-use tool for practicing engineers involved in the design, selection, integration, and retrofit of ESP components and systems to understand how VFDs can excite either the electrical resonance modes of a transmission cable or mechanical resonance modes of a rotating shaft in their systems. In this sense, it can help to avoid ESP failures that might result from a poor PQ caused by VFDs. Analytical expressions of different types of harmonics in these systems, including their interharmonics and other types of applicable common-mode harmonics, are derived to support such engineering studies and analyses. Offline and RTHS results both in time and frequency domains, as well as experimental results, have been provided to demonstrate the relevance of the proposed modeling approach. The model proposed in this article is suitable for steady-state analysis only. Therefore, transient system performance, such as the effects of the VFD controller, dynamic load change, and faults, cannot be analyzed using this model.

References

[1] L. Ding, Y. W. Li, N. R. Zargari, and R. Paes, "Sensorless control of csc-fed pmsm drives with low switching frequency for electrical submersible pump application," *IEEE Trans. Ind. Appl.*, vol. 56, no. 4, pp. 3799–3807, Jul./Aug. 2020.

[2] D. A. M. Fonsêca, A. O. Salazar, E. R. L. Villarreal, and G. A. E. Espinoza, "Downhole telemetry systems to monitor electric submersible pump parameters in oil well," *IEEE Access*, vol. 9, pp. 12824–12839, 2021.

[3] J. R. Smith, D. M. Grant, A. Al-Mashgari, and R. D. Slater, "Operation of subsea electrical submersible pumps supplied over extended length cable systems," *IEE Proc. Electr. Power Appl.*, vol. 147, no. 6, pp. 544–552, Nov. 2000.

[4] X. Liang, N. C. Kar, and J. Liu, "Load filter design method for medium-voltage drive applications in electrical submersible pump systems," *IEEE Trans. Ind. Appl.*, vol. 51, no. 3, pp. 2017–2029, May/Jun. 2015.

[5] Z. E. Al-Haiki and A. N. Shaikh-Nasser, "Power transmission to distant offshore facilities," *IEEE Trans. Ind. Appl.*, vol. 47, no. 3, pp. 1180–1183, May/Jun. 2011.

[6] O. J. Romero and A. Hupp, "Subsea electrical submersible pump significance in petroleum offshore production," *J. Energy Resour. Technol.*, vol. 136, no. 1, pp. 1–9, Sep. 2014.

[7] R. S. Minette, S. F. Silvaneto, L. A. Vaz, and U. A. Monteiro, "Experimental modal analysis of electrical submersible pumps," *Ocean Eng.*, vol. 124, pp. 168–179, Sep. 2016.

[8] M. O. Durham, R. A. Durham, and R. H. Hulett, "History and development of IEEE standards for downhole cable," *IEEE Trans. Ind. Appl.*, vol. 43, no. 2, pp. 436–443, Mar./Apr. 2007.

[9] C. Bremner *et al.*, "Evolving technologies: Electrical submersible pumps," *Oilfield Rev.*, vol. 18, no. 4, pp. 30–43, 2006.

[10] R. Pragale and D. D. Shipp, "Investigation of premature ESP failures and oil field harmonic analysis," *IEEE Trans. Ind. Appl.*, vol. 53, no. 3, pp. 3175–3181, May/Jun. 2018.

[11] M. Farbis, H. Hoevenaars, and J. L. Greenwald, "Oil field retrofit of ESPs to meet harmonic compliance," *IEEE Trans. Ind. Appl.*, vol. 52, no. 1, pp. 718–727, Jan./Feb. 2016.

[12] F. P. Feletto, R. A. Durham, E. D. C. Bortoni, and J. G. de Carvalho Costa, "Improvement of MV cascaded H-bridge inverter (CHBI) VFD availability for high-power ESP oil wells," *IEEE Trans. Ind. Appl.*, vol. 55, no. 1, pp. 1006–1011, Jan./Feb. 2019.
[13] *Design of Reliable Industrial and Commercial Power Systems (Gold Book)—Reliability*, IEEE Standard 493 2007, 2007.
[14] S. F. Rabbi and M. A. Rahman, "Equivalent circuit modeling of a hysteresis interior permanent magnet motor electric submersible pumps," *IEEE Trans. Magn.*, vol. 52, no. 7, pp. 1199–1209, Jul. 2016.
[15] M. Zafarani, B. H. Jafari, and B. Akin, "Lateral and torsional vibration monitoring of multistack rotor induction motors," *IEEE Trans. Ind. Electron.*, vol. 68, no. 4, pp. 3494–3505, Apr. 2021.
[16] S. F. Rabbi and J. T. Kahnamouei, "Shaft failure analysis in soft-starter fed electrical submersible pump systems," *IEEE Open J. Ind. Appl.*, vol. 1, pp. 1–10, Dec. 2020.
[17] A. B. Nassif, "Assessing the impact of harmonics and interharmonic of top and mudpump variable frequency drives in drilling rigs," *IEEE Trans. Ind. Appl.*, vol. 55, no. 4, pp. 5574–5583, Nov./Dec. 2019.
[18] Y. Zhang and Y. W. Li, "Investigation and suppression of harmonics interaction in high-power pwm current-source motor drives," *IEEE Trans. Power Electron.*, vol. 30, no. 2, pp. 668–679, Feb. 2015.
[19] T. Abdelazim, D. Shipp, and T. Dionise, "Reducing electrical submersible pump downtime by mitigation of VSD output power quality problems," in *Proc. IEEE Petroleum Chem. Ind. Committee Conf.*, Vancouver, BC, Canada, 2019, pp. 163–166.
[20] C. S. Mardegan and D. D. Shipp, "Anatomy of a complex electrical failure and its forensics analysis," *IEEE Trans. Ind. Appl.*, vol. 50, no. 4, pp. 2910–2918, Jul./Aug. 2014.
[21] X. Liang and A. El-Kadri, "Operational parameters affecting harmonic resonance in electrical submersible pump systems," *Can. J. Elect. Comput. Eng.*, vol. 42, no. 3, pp. 183–197, Jul. 2019.
[22] X. Liang, "Linearization approach for modeling power electronics devices in power systems," *IEEE J. Emerg. Sel. Topics Power Electron.*, vol. 2, no. 4, pp. 1003–1012, Dec. 2014.
[23] X. Han and A. B. Palazzolo, "VFD machinery vibration fatigue life and multi-level inverter effect," *IEEE Trans. Ind. Appl.*, vol. 49, no. 6, pp. 2562–2575, Nov./Dec. 2013.
[24] S. Mohamadian, A. Tessarolo, S. Castellan, and A. Shoulaie, "Steady-state simulation of LCI-fed synchronous motor drives through a computationally efficient algebraic method," *IEEE Trans. Power Electron.*, vol. 32, no. 1, pp. 452–470, Jan. 2017.
[25] SIEMENS, "Sinamics perfect harmony GH180." [Online]. Available: https://support.industry.siemens.com/cs/attachments/109761720/sinamics-perfect-harmony-gh180-catalog-d17-global-2018.pdf?download=true
[26] J. Pedra, "On the determination of induction motor parameters from manufacturer data for electromagnetic transient programs," *IEEE Trans. Power Syst.*, vol. 23, no. 4, pp. 645–652, Nov. 2008.
[27] O. V. Thorsen and M. Dalva, "Combined electrical and mechanical model of electric submersible pumps," *IEEE Trans. Ind. Appl.*, vol. 37, no. 2, pp. 541–547, Mar. 2001.
[28] G. Ekemb, F. Slaoui-Hasnaoui, J. Song-Manguelle, P. M. Lingom, and I. Fofana, "Instantaneous electromagnetic torque components in synchronous motor fed by load-commutated inverters," *Energies*, vol. 14, no. 11, pp. 1–25, May 2021.
[29] J. Song-Manguelle, S. Schröder, T. Geyer, G. Ekemb, and J. M. Nyobe-Yome, "Prediction of mechanical shaft failures due to pulsating torques of variable-frequency drives," *IEEE Trans. Ind. Appl.*, vol. 45, no. 5, pp. 1979–1988, Oct. 2010.
[30] Y. D. Baba *et al.*, "Slug translational velocity for highly viscous oil and gas flows in horizontal pipes," *Energies*, vol. 4, no. 3, pp. 1–20, Sep. 2019.
[31] C. Mung-Ong, *Dynamic Simulation of Electric Machinery Using Matlab/Simulink*. Englewood Cliffs, NJ, USA: Prentice-Hall, 1999.
[32] P. M. Lingom, J. Song-Manguelle, R. C. C. Flesch, and J. Tao, "A generalized single-carrier PWM scheme for multilevel converters," *IEEE Trans. Power Electron.*, vol. 36, no. 10, pp. 12112–12126, Oct. 2021.
[33] P. M. Lingom, J. Song-Manguelle, D. L. Mon-Nzongo, R. C. C. Flesch, and J. Tao, "Analysis and control of PV cascaded h-bridge multilevel inverter with failed cells and changing meteorological conditions," *IEEE Trans. Power Electron.*, vol. 36, no. 2, pp. 1777–1789, Jul. 2020.
[34] J. Song-Manguelle, G. Ekemb, D. Mon-Nzongo, J. Tao, and M. L. Doumbia, "A theoretical analysis of pulsating torque components in AC machines with variable frequency drives and dynamic mechanical loads," *IEEE Trans. Ind. Electron.*, vol. 65, no. 12, pp. 9311–9324, Dec. 2018.
[35] D. G. Holmes and T. A. Lipo, *Pulse Width Modulation for Power Converters, Principles and Practice*. Piscataway, NJ, USA: IEEE Press, 2003.
[36] G. W. Chang and S. K. Chen, "An analytical approach for characterizing harmonic and inter-harmonic currents generated by VSI-Fed adjustable speed drives," *IEEE Trans. Power Del.*, vol. 20, no. 4, pp. 2585–2593, Oct. 2005.
[37] D. Mon-Nzongo, G. Ekemb, J. Song-Manguelle, P. G. Ipoum-Ngome, and J. Tao, "LCIs and PWM-VSIs for petroleum industry: A torque-oriented evaluation for torsional analysis purposes," *IEEE Trans. Power Electron.*, vol. 34, no. 9, pp. 8956–8970, Sep. 2019.
[38] K. Sungil and K. Heeyoung, "A new metric of absolute percentage error for intermittent demand forecasts," *Int. J. Forecast.*, vol. 32, no. 3, pp. 669–679, Sep. 2016.
[39] National Instruments PXI-6229 Datasheet, Oct. 2021. [Online]. Available: https://www.artisantg.com/info/NI_PXI_6229_Datasheet.pdf
[40] Electric Submersible Pumps–Oil production, Jul. 2017. [Online]. Available: http://oilproduction.net/files/ALS/GE-%20ESP%20Brochure.pdf

P. M. Lingom (Student Member, IEEE) received the B.S and M.S. degrees in pedagogical sciences and electrical engineering from ENSET, University of Douala, Douala, Cameroon, in 2014 and 2016, respectively. Since September 2018, he has been working toward the Ph.D. degree with the Department of Electrical Engineering and Automation, Fuzhou University, Fuzhou, China.

His current research interests include the analysis and control of multilevel power converters for both grid-connected renewable energy systems and variable-speed drive applications.

Joseph Song-Manguelle (Senior Member, IEEE) received the B.S. and M.S. degrees in pedagogical sciences and electrical engineering from ENSET, University of Douala, Douala, Cameroon, in 1995 and 1997, respectively, and the Ph.D. degree in electrical engineering from the Swiss Federal Institute of Technology, Lausanne, Switzerland, in 2004.

From 2004 to 2012, he held engineering positions with General Electric in Germany, France, and New York, USA, where he was involved in the development of torsional vibration control systems with VFDs and HVdc transmission and distribution systems for future long tieback subsea applications; he holds four patents. From 2012 to 2021, he was a Senior Electrical Engineer and VFD Subject Matter Expert for ExxonMobil in Texas, Russia, and Papua New Guinea, involved in the technical qualification of high-power subsea electrical components facilities design, commissioning, and troubleshooting. Since 2021, he has been with Oak Ridge National Laboratory, Knoxville, TN, USA, as a Distinguished R&D Staff, developing new high-power electronics research programs for the U.S. National Transportation Research Center. In parallel to his professional activities, since 2010, he has been cosupervising master's and Ph.D. students at the University of Douala, Fuzhou University, Fujian, China, and the University of Quebec at Trois-Rivieres, Trois-Rivieres, QC, Canada, where he is an Adjunct Professor.

Dr. Song-Manguelle is an Associate Editor for the IEEE JOURNAL OF EMERGING AND SELECTED TOPICS IN POWER ELECTRONICS.

Mamadou Lamine Doumbia (Member, IEEE) received the M.Sc. degree in electrical engineering from Moscow Power Engineering Institute (Technical University), Moscow, Russia, in 1989, the M.Sc. degree in industrial electronics from the Université du Québec à Trois-Rivières (UQTR), Trois-Rivieres, QC, Canada, in 1994, and the Ph.D. degree in electrical engineering from Ecole Polytechnique de Montreal, Montreal, QC, Canada, in 2000.

From 2000 to 2002, he was a Lecturer with Ecole Polytechnique de Montreal and the CEGEP Saint-Laurent, Montreal, QC, Canada. He was a Senior Research Engineer with CANMET Energy Technology Centre, Natural Resources Canada (2002–2003) and a Researcher with the Hydrogen Research Institute (HRI) (2003–2005). Since 2005, he has been a Professor with the Department of Electrical and Computer Engineering, UQTR. He has authored or coauthored more than 100 papers in international journals and conferences. His research interests include renewable energy systems, distributed energy resources, variable speed drives, power electronics, and power quality.

Dr. Doumbia is a member of the IEEE Power Electronics Society and IEEE Communications Society. He is a Professional Engineer and a member of the Ordre des Ingenieurs du Quebec. He is currently an editorial board member of the *International Journal of Renewable Energy Research* and *International Journal of Smart Grid*.

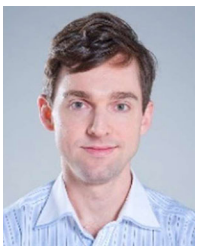

Rodolfo César Costa Flesch (Member, IEEE) received the B.E., M.Eng., and Dr.Eng. degrees in control and automation engineering from the Federal University of Santa Catarina (UFSC), Florianopolis, Brazil, in 2006, 2009, and 2012, respectively.

He is currently a Professor with the Department of Automation and Systems Engineering, UFSC, and a Researcher with the Brazilian National Council for Scientific and Technological Development, Brasília, Brazil. In addition, he is the coordinator of several R&D cooperation projects between the academy and industry. His current research interests include process control (time-delay processes and model predictive control), instrumentation, and automation of tests.

Tao Jin (Senior Member, IEEE) received the B.S. and M.S. degrees from Yanshan University, Hebei, China, respectively, in 1998 and 2001, and the Ph.D. degree from Shanghai Jiaotong University, Shanghai, China, in 2005, all in electrical engineering.

From 2005 to 2007, he was a Postdoctor with Shanghai Jiaotong University. During this time, he was in charge of a research group in the biggest dry-type transformer company in Asia, Sunten Electrical, Co., Ltd., to develop new transformer technology with a distribution grid. From 2008 to 2009, he was a Research Scientist with Virginia Tech, Blacksburg, VA, USA, where he was involved in the design and test of PMU technology and GPS/Internet-based power system frequency monitoring network. In 2010, he joined Imperial College, London, U.K., as a European Union Marie Curie Research Fellow, where he was focused on electrical technologies related to the smart grid. He is currently a Professor with the College of Electrical Engineering and Automation, Fuzhou University, Fujian, China. He has authored/coauthored about 150 papers.

Dr. Jin is a member of the IEEE Power and Energy Society and IEEE Industrial Electronics Society and a special committee member of the Chinese Society of Electrical Engineering, China Electrotechnical Society, and so on. He currently serves as an Associate Editor for the *Journal of Modern Power System and Clean Energy*, *Protection and Control of Modern Power Systems*, *China Measurement and Testing Technology*, and other journals.